An experimental and numerical study of laminar natural convection along vertical rib-roughened surfaces

Essam Nabil Ahmed [a], Giovanni Tanda [b],*

[a] *DICCA, Università degli Studi di Genova, via Montallegro 1, 16145 Genova, Italy*
[b] *DIME, Università degli Studi di Genova, via Montallegro 1, 16145, Genova, Italy*

ARTICLE INFO

ABSTRACT

Air natural convection along a vertical surface periodically roughened with wooden ribs, square in section and either spanwise-elongated or truncated and arranged in a staggered pattern, is investigated at a Rayleigh number of 2×10^7, which corresponds to a stable buoyant air flow. The influence of roughness on local and overall convective heat transfer was analyzed experimentally via schlieren imaging and extensive energy balance calculations and numerically through both conventional and homogenization-based CFD (computational fluid dynamics) simulations. For the considered range of the rib pitch-to-height ratio (from 3.5 to 20), the continuous, transverse elements were generally found to degrade the local and overall convective heat transfer, with the deterioration becoming more pronounced when the ribs are densely packed on the surface. Furthermore, even staggered truncated ribs failed to provide any local/overall enhancement to convective heat transfer. The simulations performed via the homogenization-based treatment, which represents an easier alternative to the standard fine-grained numerical analysis, led to heat transfer trends in line with those obtained by fully resolving simulations and experiments. Both numerical approaches showed that the conjugate heat transfer problem must be tackled in the case of low-thermal-conductivity ribs since the solution, in terms of heat transfer characteristics, is intermediate between the cases of adiabatic and perfectly conducting elements.

1. Introduction

Natural convection heat transfer from vertical ribbed surfaces is relevant to a wide range of applications such as electronic equipment cooling [1], photovoltaic and thermal solar systems [2], passive solar heating and ventilation of buildings [3,4], heat removal in nuclear technology [5], and many others. There are situations where roughness or obstacles are present naturally (or to perform functions related to the specific application, without paying primary attention to their impact on heat transfer) and others in which they are added intentionally to alter the buoyant-flow behavior and the heat transfer characteristics, for instance by producing physical disturbances in the laminar boundary layer which may stimulate an earlier transition to turbulence and, therefore, lead to an enhancement of the heat transfer performance. The former may be the case of electronic circuit boards or even surfaces of buildings, while passive solar systems and photovoltaic modules are examples of the latter. In both cases, a proper understanding of the flow and thermal behavior of these systems is essential for their design.

As widely discussed in the literature, roughness elements over a vertical surface may induce marked modification to the buoyant flow and, at the same time, add an extra heat transfer area. Although the increase in surface area is clearly beneficial to the heat transfer rate exchanged with the convective fluid, the effectiveness of roughness elements in enhancing the heat transfer coefficient is intriguingly controversial, with some studies indicating a slight increase (relative to the smooth surface) in limited circumstances (e.g., zigzag-shaped surfaces [6], stepped surfaces [7], and truncated rib elements [8]) and others finding a general reduction, as in the case of repeated spanwise-elongated ribs of square cross section [7,9], due to the presence of stagnation zones just up- and downstream of the ribs, which result in local thickening of the thermal boundary layer. For some roughness geometries, the combined effect of the increase in surface area and the decrease of the heat transfer coefficient yields, eventually, an enhancement of the heat transfer rate (for example, complex wavy surfaces [10]).

Provided that in the laminar flow regime the surface roughness elements have a limited influence (negative in most cases) on the local heat

---

* Corresponding author.
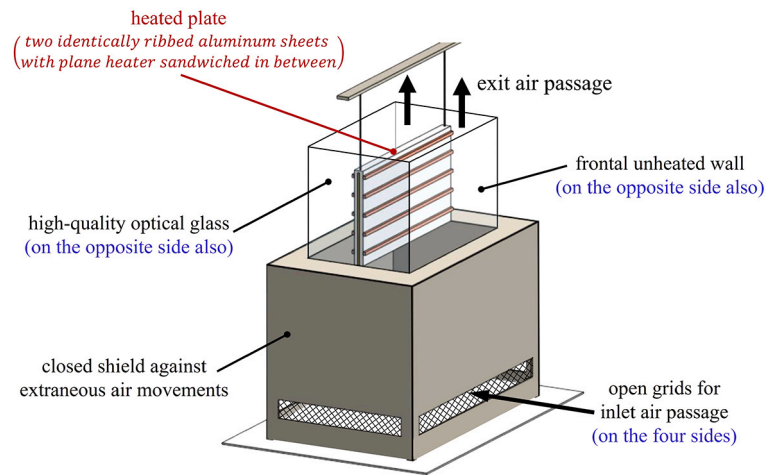*E-mail address:* giovanni.tanda@unige.it (G. Tanda).

Fig. 1. Schematic layout of the experimental test section.

transfer coefficient (as indicated, for instance, by Fujii et al. [11]), a perspective of heat transfer enhancement may be related to the chance of triggering the transition to turbulence at lower Rayleigh numbers relative to the smooth surface case, as argued by Bhavnani and Bergles [12] and Yao [10]. In recent experimental papers, Tanda et al. [8,13] found that the use of truncated ribs (in lieu of continuous ones), with a proper length of the rib segments and at a Rayleigh number close to that characterizing the upper threshold of the laminar regime over a corresponding smooth plate, was able to provide an increase in the heat transfer coefficient averaged over the inter-rib regions (the only portions along which the heat transfer coefficient was detected by the employed optical technique) of up to 8% relative to the smooth surface, with the peaks higher by 15% or more on a local basis. It is deemed that the relative enhancement would be markedly higher if the contribution of rib surfaces were accounted for. The investigation of the thermal boundary layer by means of schlieren visualization and miniature thermocouple measurements indicated the presence of local flow unsteadiness in isolated spots (in particular, close to the segment edges); this phenomenon, combined with a possibly favorable redistribution of the main buoyant flow due to the presence of rib protrusions, was conjectured to be responsible for the recorded enhancement of the heat transfer coefficient.

The present study is aimed at investigating, through a combined experimental-numerical framework, the same roughness geometries (continuous and truncated ribs) explored in Refs. [8,13], yet under conditions, here, well within the laminar regime (by using a plate with a shorter vertical length and imposing an appropriate wall-to-fluid temperature difference). Since some optimized roughness geometries (e.g., truncated rib elements with a proper length) were found in Refs. [8,13] beneficial for heat transfer coefficient enhancement when working close to the transitional regime, the crux of the present contribution is whether the imposition of a stable flow would guarantee, for the same geometries, superior heat transfer performance relative to the smooth plate. Besides the experimental survey in which the schlieren optical technique is employed together with energy balance calculations, carrying out the study under the laminar flow regime facilitates performing numerical simulations of the conjugate heat transfer problem (thermal conduction through ribs and natural convection from the ribs and the inter-rib portions of the baseplate to air) through conventional CFD tools as well as the homogenization-based treatment. The latter provides, via upscaling, a computationally cheaper alternative to the standard full feature-resolving simulation over regularly microstructured vertical surfaces. The reader is referred to Refs. [14–16] in which the homogenized model was formulated and implemented on relevant cases, at earlier stages of this research project.

The paper is structured as follows. In Section 2, the experimental procedure and the main quantities recorded (local and overall heat transfer coefficient) are outlined. Section 3 addresses features of the fine-grained CFD analysis and, then, describes the homogenization approach with focus on the definition of the effective boundary conditions to be imposed and the evaluation of the upscaled coefficients of interest. The results are presented and discussed in Section 4, while the main findings of the study are highlighted in Section 5.

2. Experimental setup and procedure

The description of the experimental test section is facilitated by the sketches in Figs. 1 and 2, showing a three-dimensional view of a representative vertical plate equipped with transverse ribs and the geometric details of rib configurations, respectively. The plate (termed "heated plate") was made of two aluminum sheets with a plane heater sandwiched in between. The sandwich principle was adopted to provide, once the electric power has been supplied to the heater, a symmetrical heat transfer on both sides of the plate. The dimensions of the heated plate are: overall thickness $t = 12$ mm, height $H = 175$ mm, and spanwise length $L = 300$ mm. The length L was chosen such that it is much greater than the other two dimensions to favor a two-dimensional thermal field and to improve the resolution of the optical method employed to deduce local heat transfer characteristics. The thickness of each sheet was sufficient to ensure, combined with the high thermal conductivity of aluminum, an efficient redistribution of heat by conduction within the plate; for this reason, the plate material was expected to be virtually isothermal. Six fine-gauge thermocouples, calibrated to ± 0.1 K, were embedded in the wall at different elevations, spanning the whole height of the heated plate, to verify temperature uniformity and to provide the mean value of the wall temperature, assumed to be the mean of the individual readings. For all the experimental runs, the temperature readings were uniform within $\pm 2\%$ of the mean plate-to-ambient temperature difference. Three additional thermocouples were located in the ambient air, sufficiently far from the heated plate, to provide a realistic measurement of the ambient air temperature and to detect any air thermal gradient in the vertical direction. Since the temperature difference among the air temperature readings provided by the three sensors was always less than 0.2 K, their average was assumed as representative of the ambient air temperature. Further, a miniature thermocouple with an exposed junction, capable of traveling along the direction normal to the plate surface ($\hat{y}$) at an arbitrary position along the vertical and spanwise coordinates ($\hat{x}$, $\hat{z}$), was used to monitor the air temperature history at selected stations inside the boundary layer in order to gain insights into the features of the thermal field and the nature of the flow regime (Refs. [8,13] can be consulted for further details).
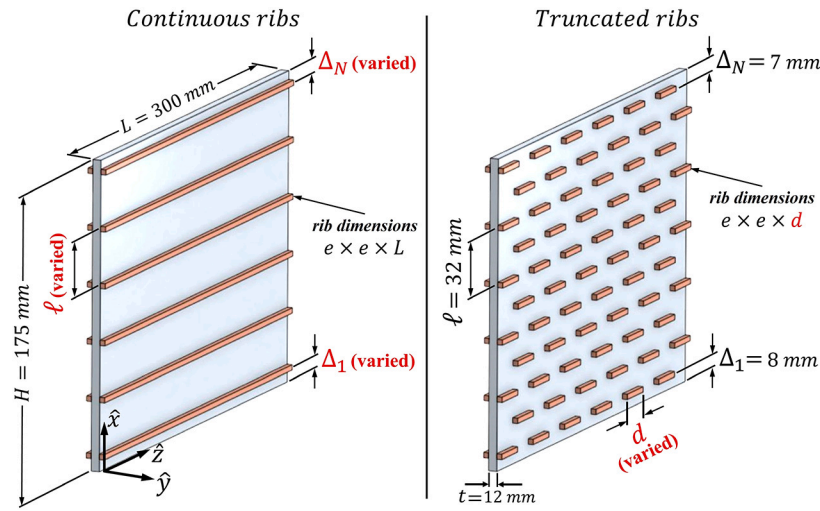
Fig. 2. The tested heated plate with continuous and truncated ribs.

Table 1
Description of rib configurations and main geometric parameters.

Rib type	Config.	Number of rows	Number of truncated ribs per row	Δ_1 (mm)	Δ_N (mm)	ℓ (mm)	d (mm)	ℓ/e	d/ℓ	H/ℓ
continuous	A1	5	-	8	7	40	-	20	-	4.38
continuous	A2	9	-	8	7	20	-	10	-	8.75
continuous	A3	17	-	8	7	10	-	5	-	17.5
continuous	B1	6	-	8	7	32	-	16	-	5.47
continuous	B2	11	-	8	7	16	-	8	-	10.94
continuous	B3	21	-	8	7	8	-	4	-	21.88
continuous	C1	7	-	4	3	28	-	14	-	6.25
continuous	C2	13	-	4	3	14	-	7	-	12.5
continuous	C3	25	-	4	3	7	-	3.5	-	25
truncated	-	11	3	8	7	32	50	16	1.56	5.47
truncated	-	11	6	8	7	32	25	16	0.78	5.47
truncated	-	11	12	8	7	32	12.5	16	0.39	5.47

Ambient air, at a temperature of 293 K (with a maximum variation of ± 1 K from one test to another), enters from the lower side of a shielding (cf. Fig. 1), whose function is to exclude possible air movements which are present in the laboratory room. For the same reason, at the top section of the shielding, the heated plate was delimited laterally by high-quality glasses (to permit optical access to the test section) and frontally by two smooth and unheated vertical walls, located at distances equal to half the plate height. According to the previous study by Tanda [9], a relatively large channel spacing-to-height ratio ($= 0.5$) is expected to have almost no influence on the heat transfer behavior along the plate relative to the case of an unconfined, isothermal, vertical plate.

Experiments were performed both in the absence and in the presence of the roughness elements on the heated plate surfaces. The ribs, made of wood, were square in section, with height e equal to 2 mm. Ribs, when present, were symmetrically attached on both sides of the heated plate at equal intervals, which were varied from one experiment to another such that a range of the ratio between the rib pitch ℓ and the rib height e extending from 20 to 3.5 was covered; this corresponded to increasing the number of ribs on each side from 5 to 25. The majority of experiments considering the heated ribbed plate were conducted by using continuous, spanwise-elongated ribs. Additional experiments were carried out with truncated ribs, in order to investigate their potential to promote the heat transfer relative to the plate with continuous ribs and the smooth plate. A single value of the rib pitch-to-height ratio and three different values of the segment length, d, were considered for the truncated elements. Dimensional characteristics of the rib configurations are shown in Fig. 2 and summarized in Table 1.

For each surface geometry, experimental runs were performed by adjusting the power input to the heater in order to maintain, when the steady state is attained, a mean plate-to-ambient temperature difference of 45 K, leading to a Rayleigh number Ra (based on the plate height H) equal to 2×10^7, where $Ra = g\beta(\hat{T}_w - \hat{T}_\infty)H^3/(\nu\alpha)$. In the previous expression, $\hat{T}_w$ and $\hat{T}_\infty$ are the baseplate wall and the ambient air temperatures, respectively, g is the gravitational acceleration, while β, α, and ν denote the thermal expansion coefficient, the thermal diffusivity, and the kinematic viscosity, respectively. Air properties were evaluated at the film temperature, that is $\hat{T}_{film} = (\hat{T}_w + \hat{T}_\infty)/2$, except for β, evaluated at the ambient air temperature. At the Rayleigh number considered (2×10^7), the flow was laminar and stable, as confirmed by measurements of the air temperature history in the boundary layer and by visualizations obtained through the schlieren optical technique described in Section 2.1. To ensure the repeatability of the experimental results, each test was repeated two or three times. Results, in terms of natural-convection, local and average heat transfer coefficients, were provided via two different approaches: local heat transfer coefficients along the surfaces (not covered by ribs) were deduced by the schlieren optical method, whereas average (overall) heat transfer coefficients along the entire rib-roughened surface (inclusive of ribs) were provided by exploitation of the energy balance based on the known input power and the calculated radiant heat exchange with the surroundings.
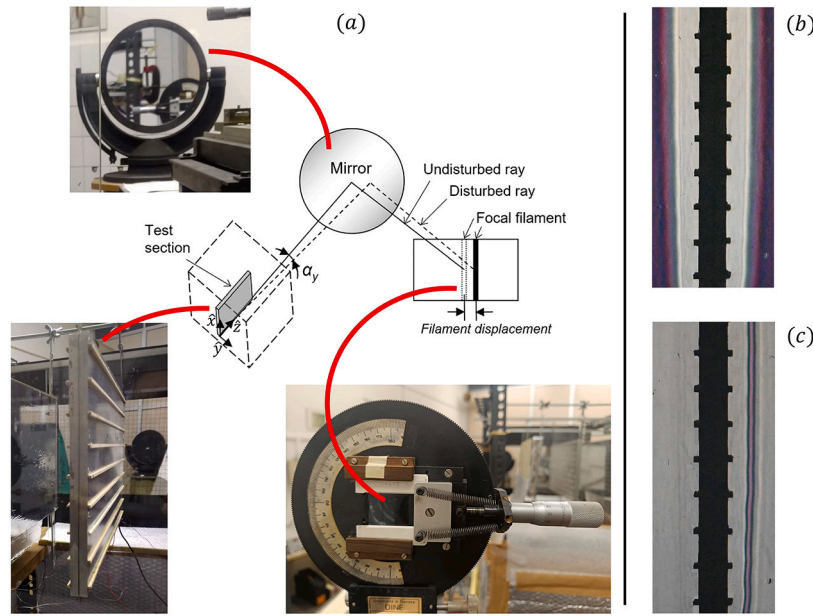
Fig. 3. Illustration of the schlieren imaging method adopted. In panel (*a*), a simple sketch describing acquisition of light ray angular deflection is provided, besides typical photos of one of the test surfaces, the concave mirror, and the movable filter connected to a micrometer. The schlieren images presented show the optical field when the filament is positioned at the focus of schlieren mirror (frame *b*), and when it is displaced to intercept deflected light rays at a given angular deflection (frame *c*). (For interpretation of the colors in the figure, the reader is referred to the web version of this article.)

2.1. Local heat transfer measurements

A schlieren optical system was used to visualize the thermal boundary layer and to evaluate the natural convection local heat transfer coefficient. An exhaustive description of the schlieren apparatus employed is given in Refs. [9,17–19]. Basically, it consists of a white light beam (composed of parallel rays) crossing the test section, a concave mirror (i.e., the schlieren mirror), which focuses the light onto its focal plane (i.e., the cut-off plane), a filter, and a camera to acquire a real image of the test section. As shown in Fig. 3, when a focal filament (for instance, a thin dark strip or wire) is used as a filter, and no thermal gradients are present in the air crossed by the light beam, all light rays are intercepted by the filter when it is placed on the focus of mirror (and the image formed on the camera will be uniformly dark). When thermal gradients (in the $\hat{y}$-direction of Fig. 3) are present, individual light rays undergo angular deflections whose extent is related to the magnitude of the gradient; consequently, the corresponding spots appear bright in the camera, permitting a reliable visualization of the thermal boundary layer (more precisely of all air particles with a non-zero thermal gradient). The angular deflection α_y of a given light ray (i.e., passing through a given point of coordinates $\hat{x}$, $\hat{y}$) can be measured by moving the filter (connected to a micrometer) along the focal plane of the schlieren mirror until the point of interest appears colored by the same color adopted for the filter (consisting of a thin transparent violet strip for these experiments). It can be demonstrated that the angular deflection α_y is given by the ratio between the filter displacement and the focal length of the mirror (since the angular deviation is small, $\tan \alpha_y \approx \alpha_y$) [20].

The local heat transfer coefficient at a point on the vertical baseplate surface is introduced, conventionally, as follows:

$$h = -k_{air,w} \frac{(\partial \hat{T}/\partial \hat{y})_w}{\hat{T}_w - \hat{T}_\infty},$$ (1)

where $(\partial \hat{T}/\partial \hat{y})_w$ is the air temperature gradient in the wall-normal direction, $\hat{y}$, evaluated at the point of interest on the baseplate, and $k_{air,w}$ is the air thermal conductivity evaluated at the wall temperature. Due to the relation between the angular deflection of light and the thermal gradient in the fluid crossed, the heat transfer coefficient, h, can be directly calculated by measuring the deflection of light passing in the

vicinity of the wall, using the following formula (refer to, for instance, Ref. [9]):

$$h = \frac{k_{air,w} \, \alpha_{y,w} \, \hat{T}_w^2}{K(\hat{T}_w - \hat{T}_\infty)},$$ (2)

where $\alpha_{y,w}$ is the angular deflection, along the $\hat{y}$-direction, of the light ray passing in the vicinity of the wall at the desired location, and K is a constant (equal to about 0.024 mK in these experiments) which depends on some air properties (Gladstone-Dale and ideal gas constants, index of refraction, pressure) and the length of the plate in the direction of light beam propagation ($\hat{z}$-coordinate in Figs. 2 and 3). Equation (2) provides values of the local heat transfer coefficient for a vertical surface, which depend on the thermal gradients in the $\hat{y}$-direction (whose effect is implicitly included via the consequent angular deflections $\alpha_{y,w}$). In this research, attention is focused on the vertical inter-rib regions of the plate; hence, the angular deviation along the $\hat{y}$-direction is the only optical data on which the heat transfer coefficient depends. Moreover, Equation (2) assumes the thermal field to be two-dimensional, i.e., independent of the $\hat{z}$-coordinate; otherwise, it is still valid, but the calculated heat transfer coefficient should, then, correspond to the value averaged along the plate spanwise length L. This implies that any three-dimensional feature of the flow emerging from the insertion of ribs can be visualized, via the current technique, only in a corresponding two-dimensional ($\hat{x}$-$\hat{y}$) domain with the results at each point averaged over a line extending in $\hat{z}$. Finally, in order to present the results in dimensionless form, the local Nusselt number was introduced as follows:

$$Nu = \frac{h \, H}{k_{air}},$$ (3)

with k_{air} the thermal conductivity of air evaluated at the film temperature.

2.2. Overall heat transfer measurements (convection and radiation components)

The overall, combined-mode (convection and radiation) heat transfer rate was determined by an energy balance. With reference to Fig. 4, the surfaces of the heated plate exposed to the environment are those
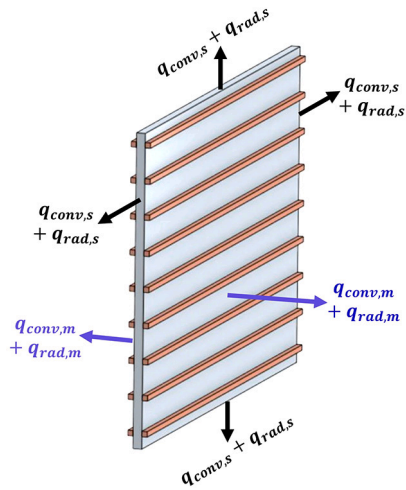
Fig. 4. Sketch illustrating the convective (subscript conv) and radiant (subscript rad) heat transfer components from the main surfaces of the heated plate (subscript m) and from the sides generated by the plate thickness (subscript s).

Fig. 5. Sketch of the calculation domain for the radiant heat transfer component from the main surface, $q_{rad,m}$.

generated by the plate thickness (four surfaces having an overall area of $2 \times t(H+L)$ and performing always in the same manner, regardless of the presence of ribs or not) and those washed by the main buoyant air flow (two surfaces having an overall area equal to $2 \times (HL)$ in the absence of ribs, while the area increases as a function of the number of continuous or truncated ribs when they are attached to the surfaces). To facilitate the description of the convective and radiant overall components, q_{conv} and q_{rad}, respectively, the subscripts m (main) and s (side) have been added based on whether the main surface area (where ribs are located) or the side area generated by the plate thickness is considered (see Fig. 4). Hence, at the steady state, the known electrically supplied power q_{el} is entirely dissipated into the environment according to the following equation:

$$q_{el} = q_{conv,m} + q_{rad,m} + q_{conv,s} + q_{rad,s}. \tag{4}$$

As the convective component from the main surfaces $q_{conv,m}$ is the quantity of major interest in this study, the remaining convection heat transfer rate $q_{conv,s}$ from the sides of the plate as well as the radiant components from all surfaces ($q_{rad,m} + q_{rad,s}$) must be calculated separately.

First, attention is given to heat transfer rate from the surfaces associated with the plate thickness: these surface areas are approximately 10% (or less in the presence of ribs) of the area ascribed to the main surfaces. For the radiant component, $q_{rad,s}$, the simple formula giving the radiation heat transfer between two gray surfaces (the thin side surface of the plate and a surrounding ideal surface taken at the ambient temperature) has been considered, with the thermal emittance of aluminum assumed to be equal to 0.12; cf. Ref. [9]. For the convective component $q_{conv,s}$, literature relationships for isothermal vertical and horizontal surfaces are expected to be unreliable due to the shape of the surfaces (with one side much larger than the other one) and their positioning (the vertical surfaces are facing the side glasses at a distance of few millimeters and not washed by an external buoyant flow): for these reasons, $q_{conv,s}$ was estimated from experiments conducted with the smooth heated plate simply by subtracting the overall radiation $q_{rad,m} + q_{rad,s}$ (straightforward to be estimated due to the simple geometry, and of limited amount due to the relatively low thermal emittance of aluminum) plus the convective component $q_{conv,m}$ (evaluated based on the integration of the local heat transfer coefficient distribution obtained by the schlieren method which can cover the entire surface when no ribs are attached) from the electrically supplied power. This procedure yielded for $q_{conv,s}$ a value of 1.8 W, which applies to all experiments (with and without ribs) conducted under the requirement of constant wall-to-ambient air temperature difference (45 K). This marginal heat transfer rate corre-
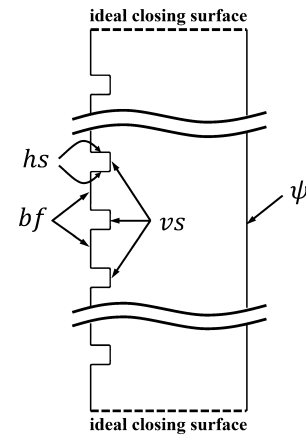
sponds to about 5% of the overall power dissipated from the heated plate. Therefore, attention is directed mainly to the calculation of the radiant heat transfer rate for the ribbed surface, in order to extract the quantity $q_{conv,m}$ of primary interest.

Whereas the estimation of $q_{rad,s}$ is relatively straightforward (and the calculated quantity is almost negligible), the calculation of the radiant component for the main surfaces ($q_{rad,m}$) is an extremely complex undertaking when ribs are present, and the modeling task necessarily requires simplifying assumptions. An analytical scheme for determining the radiation heat transfer has been developed, using a diffuse, gray-body network, which includes interactions between the heated plate (i.e., each side of the wooden ribs and the inter-rib aluminum surfaces) and the surrounding (i.e., the frontal unheated walls and the laboratory environment). As illustrated in Fig. 5, the plate surface with ribs comprises elements (assumed at uniform temperature, irradiance and radiosity within the respective areas and considered as gray and diffuse bodies) that behave differently from each other due to a different exposition and/or surface temperature and/or thermal emittance: the inter-rib surfaces of the baseplate directly exposed to the fluid (bf), the vertical sides of ribs (vs), and the horizontal sides of ribs (hs). The elements seen by the heated plate are the frontal unheated walls (ψ) and the ideal closing surfaces which delimit the enclosure from the top and the bottom. Configuration factor algebra [21] was employed to calculate the configuration factors among the surfaces involved in the radiant heat exchange, making use of basic configuration factors such as a pair of parallel rectangles situated one above the other, or a pair of perpendicular rectangles sharing a common edge. Further assumptions are listed as follows: (i) the third (spanwise) dimension is assumed to be infinite to simplify the gray-body network; (ii) the wall temperature of each inter-rib aluminum surface is equal to the experimentally evaluated mean wall temperature $\hat{T}_w$; (iii) temperature of the surrounding surfaces is equal to the experimentally evaluated ambient air temperature $\hat{T}_\infty$; (iv) mean temperature of the rib surfaces $\hat{T}_{rib}$ is given by the empirical relationship $\hat{T}_{rib} = \hat{T}_\infty + \Theta(\hat{T}_w - \hat{T}_\infty)$, where Θ was set to 0.85, according to detailed infrared thermography measurements performed at the steady state; (v) values of the thermal emittance of aluminum surfaces (0.12), wooden rib surfaces (0.9), and unheated wall surfaces facing the heated plate (0.25) were taken from the literature [9,22], while the radiosity of the laboratory room surfaces was imposed to be $\sigma \hat{T}_\infty^4$, where σ is the Stefan-Boltzmann constant.

Once the convective and radiant components $q_{conv,s}$, $q_{rad,s}$, and $q_{rad,m}$ were calculated, the convective heat transfer rate from the main sides of the heated plate, $q_{conv,m}$, was directly obtained from Eq. (4). The average convective Nusselt number, $\overline{Nu}$, is expressed as

$$\overline{Nu} = \frac{q_{conv,m}}{2HL(\hat{T}_w - \hat{T}_\infty)} \times \frac{H}{k_{air}}. \tag{5}$$

Since the nominal area chosen in the aforementioned expression (= $2HL$) is fixed regardless of the actual heat transfer area which depends on the number of ribs attached, the comparison of results based on $\overline{Nu}$ directly reflects the trends of $q_{conv,m}$ for the different configurations tested (see Table 1), which includes, by definition, the effect of surface area increase due to the presence of ribs.

To permit quantification of the impact of the radiant component $q_{rad,m}$ relative to the convective one, the average radiant Nusselt number was introduced as

$$\overline{Nu}_{rad} = \frac{q_{rad,m}}{2HL(\hat{T}_w - \hat{T}_\infty)} \times \frac{H}{k_{air}}. \tag{6}$$

The comparison between $\overline{Nu}_{rad}$ and $\overline{Nu}$ permits us to infer the role exerted by the two mechanisms. The radiant component is expected to be very little when ribs are absent or largely spaced; conversely, convective and radiant components tend to equalize when more ribs are densely fitted on the heated plate, as discussed later in Section 4.

2.3. Experimental uncertainty

The calculation of uncertainty in results of the main quantities (at the 95% confidence level) was performed according to the procedure outlined in Ref. [23]. In principle, the uncertainty in the local heat transfer coefficient h (deduced by the schlieren method), and consequently in the local Nusselt number Nu, is related to accuracy of the measurements of (i) the angular deflection of light rays passing in the vicinity of the plate surface, (ii) the wall absolute temperature, and (iii) the wall-to-ambient temperature difference, as can be inferred from Eq. (2). According to the root-sum square combination of the effects of each of the individual uncertainties [23], the dominant role is played by the uncertainty associated with the optical measurement, much larger than those related to the wall temperature and the wall-to-ambient temperature difference. In particular, the larger the recorded angular deflection, the smaller the error in the associated heat transfer coefficient. Based on the range of detected angular deflections, the uncertainty in h values was estimated to fall into the ± 9–12% range. The uncertainty in the average convective Nusselt number was calculated to be only $\pm 4\%$ for the smooth surface, while, for the ribbed surface, it can be considerably affected by the error in the calculation of radiation heat transfer from ribs. The latter accounts for the uncertainty in the emittance of materials (aluminum, wooden ribs, and shrouding walls) and the approximation errors introduced by the methodology for the radiant component evaluation. The calculated uncertainty for the radiant component (i.e., the average radiant Nusselt number) was $\pm 14\%$; since the contribution of radiation is expected to equalize, in the worst case, the convective one, the uncertainty in the average (convective) Nusselt number ranged from $\pm 4\%$ (for the smooth surface case) to $\pm 14\%$ (with the densest roughness pattern). Finally, the uncertainty associated with the Rayleigh number, mainly dependent on errors in the wall-to-ambient temperature difference, was estimated to be $\pm 2.5\%$.

3. Numerical modeling and homogenization procedure

3.1. The feature-resolving simulations

The computational domains for the two- and the three-dimensional fine-grained simulations, those involving full resolution of the fields near and within the typical corrugations of the ribbed surface, are sketched in Fig. 6(a, b). Steady conjugate natural convection is considered along the vertical plate since (i) the analysis takes place after balance is reached between the heat supplied to the baseplate and the heat dissipated to air, and (ii) the flow is assumed laminar (at $Ra \approx 2 \times 10^7$), based on schlieren observations and thermocouple measurements available from the present experiments. Under a uniform, time-independent baseplate wall temperature $\hat{T}_w \approx 338$ K and with the ambient temperature $\hat{T}_\infty \approx 293$ K (values imposed in conformity with experiments),

the value of the criterion $\beta(\hat{T}_w - \hat{T}_\infty)$ is around 0.15 (β is the thermal expansion coefficient), much smaller than 1. The Boussinesq approximation is therefore assumed to be valid [6]; it is applied here employing a linear temperature-density relationship. The conservation equations governing the spatial distribution of the velocity vector, $\hat{u}_i$, and the temperature, $\hat{T}$, in the fluid domain are

$$\frac{\partial \hat{u}_i}{\partial \hat{x}_i} = 0, \tag{7}$$

$$\rho \hat{u}_j \frac{\partial \hat{u}_i}{\partial \hat{x}_j} = -\frac{\partial(\hat{P} - \hat{P}_\infty)}{\partial \hat{x}_i} + \mu \frac{\partial^2 \hat{u}_i}{\partial \hat{x}_j^2} + \rho\beta(\hat{T} - \hat{T}_\infty)g\,\delta_{i1}, \tag{8}$$

$$\hat{u}_j \frac{\partial \hat{T}}{\partial \hat{x}_j} = \alpha \frac{\partial^2 \hat{T}}{\partial \hat{x}_j^2}, \tag{9}$$

where $\hat{P}_\infty$, g, and δ_{ij} are, respectively, the pressure in the stagnant region sufficiently far away from the wall, the magnitude of the gravitational acceleration, and the Kronecker delta function. To facilitate the reading of governing equations, $\hat{x}$, $\hat{y}$ and $\hat{z}$ coordinates were indicated in this section as $\hat{x}_1$, $\hat{x}_2$ and $\hat{x}_3$, respectively. Again, as in Section 2, the air density (ρ), dynamic viscosity (μ), thermal conductivity (k_{air}), and thermal diffusivity (α) are evaluated at the film temperature, while the volumetric thermal expansion coefficient (β) is evaluated at the ambient temperature. Steady thermal conduction takes place through the roughness elements; the temperature distribution in the ribs, $\hat{\mathcal{T}}(\hat{x}_i)$, is governed by the Laplace's equation

$$\frac{\partial^2 \hat{\mathcal{T}}}{\partial \hat{x}_j^2} = 0. \tag{10}$$

The temperature boundary conditions at the base-fluid interface ($\mathcal{I}_{bf}$), the base-rib interface ($\mathcal{I}_{br}$), and rib-fluid interface ($\mathcal{I}_{rf}$) are

$$\begin{cases} \hat{T} = \hat{T}_w & \text{at } \mathcal{I}_{bf}, \\ \hat{\mathcal{T}} = \hat{T}_w & \text{at } \mathcal{I}_{br}, \\ \hat{T} = \hat{\mathcal{T}}, \ \frac{\partial \hat{T}}{\partial \hat{n}} = \kappa \frac{\partial \hat{\mathcal{T}}}{\partial \hat{n}} & \text{at } \mathcal{I}_{rf}, \end{cases} \tag{11}$$

with $\kappa = \frac{k_{rib}}{k_{air}} \approx 3.66$ the rib-to-fluid (wood-to-air) thermal conductivity ratio and $\hat{n}$ the dimensional distance in the direction normal to $\mathcal{I}_{rf}$ at any point. No-slip velocity boundary conditions are imposed at $\mathcal{I}_{rf}$ and $\mathcal{I}_{bf}$. In addition, uniform pressure boundary conditions are defined at the inlet ($\hat{x}_1 = 0$) and the outlet ($\hat{x}_1 = H$), satisfying an equilibrium with the hydrostatic pressure head, for the flow to be driven purely by the buoyant force. At the far boundary (located at $\hat{y} = \mathcal{O}(H)$), the boundary conditions $\frac{\partial \hat{T}}{\partial \hat{x}_2} = \frac{\partial \hat{u}_1}{\partial \hat{x}_2} = 0$ and $\hat{u}_2 = 0$ are smoothly attained.

All the simulations were run using Simcenter STAR-CCM+ 2302 software (version 18.02.008-R8). The numerical procedure is similar to that adopted in Ref. [16], at an earlier stage of this project. The surface-averaged Nusselt number, $\overline{Nu}$, was used as a criterion for convergence of the solution. At any point on the ribs or on the inter-rib regions of the baseplate, the local Nusselt number, Nu, is evaluated as follows:

$$Nu = \frac{-H}{\hat{T}_w - \hat{T}_\infty} \times \frac{\partial \hat{T}}{\partial \hat{n}}\bigg|_{wall}. \tag{12}$$

The average Nusselt number is calculated, throughout this article, by integrating Nu over the area of the surfaces exposed to natural convection, i.e., the interfaces $\mathcal{I}_{bf}$ and $\mathcal{I}_{rf}$, while using the baseplate area ($\hat{\mathcal{A}}_{base}$), which is the same for all configurations including the smooth surface case, as a weight:

$$\overline{Nu} = \frac{1}{\hat{\mathcal{A}}_{base}} \int_{\mathcal{I}_{bf} + \mathcal{I}_{rf}} Nu\, d\hat{S}, \tag{13}$$

where $d\hat{S}$ is, ideally, an infinitesimal surface area. Since the computational domains considered for the different patterns of truncated ribs
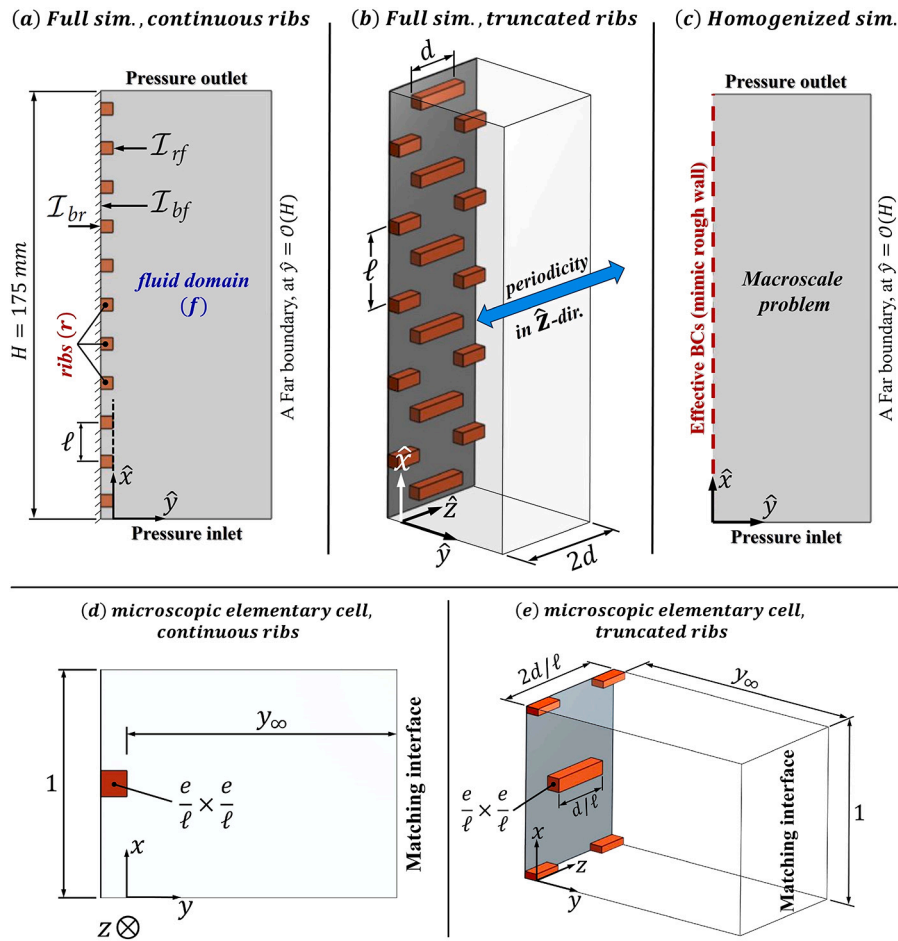
Fig. 6. Sketches of the computational domains considered for different numerical simulations: (*a*) case of spanwise-elongated ribs, a two-dim. problem; (*b*) case of truncated ribs, a three-dim. problem; (*c*) homogenized simulation. An elementary cell of the microscopic subdomain near the continuous ribs is presented in panel (*d*), while that for truncated ribs is shown in panel (*e*), both sketched in the dimensionless coordinates $x_i = \hat{x}_i/\ell$.

are three dimensional with periodicity of the fields in the spanwise direction over a distance equal to $2 \times d$, as shown in Fig. 6(*b*), Equation (13) reads

$$\left.\overline{Nu}\right|_{3D\ patterns} = \frac{1}{2d \times H} \int_{\mathcal{I}_{bf}+\mathcal{I}_{rf}} Nu\, d\hat{S}, \qquad (14)$$

while two-dimensional ($\hat{x}$–$\hat{y}$) computational domains are considered for surfaces roughened with continuous ($\hat{z}$-elongated) ribs, and the definition of $\overline{Nu}$ thus reduces to

$$\left.\overline{Nu}\right|_{2D\ patterns} = \frac{1}{H} \int_{\mathcal{I}_{bf}+\mathcal{I}_{rf}} Nu\, d\hat{s}, \qquad (15)$$

with $\hat{s}$ a distance that goes along the base-fluid and the rib-fluid interfaces.

Finally, to enhance reproducibility of the numerical results, we indicate that extra mesh refinement close to the leading edge of the vertical plate (where thickness of the thermal boundary layer is significantly small) was avoided by calculating the average Nusselt number over the region $0 \le \hat{x}_1/H \le 0.01$ of the baseplate surface (i.e., up to $\hat{x}_1 = 1.75$ mm) based on the correlation proposed by Churchill and Chu [24] (the one proved to be valid over the full laminar flow range including when the corresponding Rayleigh number tends to *zero*, such as in the neighborhood of the leading edge) instead of evaluating it from the simulations; the reader is referred to the relevant implementation in Ref. [16].

3.2. The homogenization-based simulations

The homogenization-based simulations are concerned with the macroscale behavior of the fluid flow over the ribbed vertical wall, by evaluating the macroscopic fields ($\ddot{u}_i, \ddot{T}, \ddot{P}$) rather than the fully-featured ones ($\hat{u}_i, \hat{T}, \hat{P}$) which are resolved in the fine-grained simulations. Taking the case of a wall roughened with truncated ribs of pitch distances $\ell_x = \ell$ and $\ell_z = 2d$ (refer to Fig. 6(*b*)) as an example, one can define the upscaled fields at a point $\Phi : (\hat{x}_\phi, \hat{y}_\phi, \hat{z}_\phi)$, located in the fluid domain beyond the roughness layer (i.e., $\hat{y}_\phi > 0$), by averaging the corresponding fully featured fields over a rectangular $\hat{x} - \hat{z}$ region whose dimensions are $\ell_x \times \ell_z$ and whose center is the point Φ, that is

$$\ddot{T}(\hat{x}_\phi, \hat{y}_\phi, \hat{z}_\phi) = \frac{1}{\ell_x \times \ell_z} \int_{\hat{x}_\phi-\ell_x/2}^{\hat{x}_\phi+\ell_z/2} \left[\int_{\hat{z}_\phi-\ell_z/2}^{\hat{z}_\phi+\ell_z/2} \hat{T}(\hat{x}, \hat{y}_\phi, \hat{z})\, d\hat{z} \right] d\hat{x}, \qquad (16)$$

and likewise for $\ddot{u}_i$ and $\ddot{P}$. Although interaction between the buoyancy-driven flow and the truncated elements under study is clearly three-dimensional, the phenomena encountered are two-dimensional when analyzed from a macroscopic perspective; they are the variation of the velocity and temperature in the wall-normal direction, $\hat{y}$, and the developing of the boundary layers in the vertical direction, $\hat{x}$. Furthermore, the spanwise velocity component vanishes upon averaging, i.e., $\ddot{u}_3 = 0$. The homogenized simulations are, therefore, run over an $\hat{x} - \hat{y}$ fluid domain, as sketched in Fig. 6(*c*), where the spatial variations of $\ddot{u}_1, \ddot{u}_2$, and $\ddot{T}$ are governed by
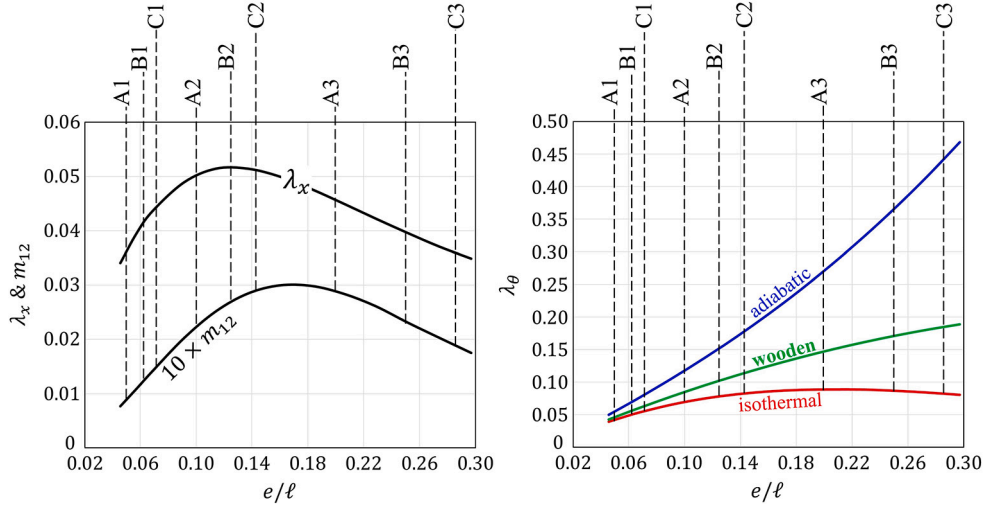
Fig. 7. Upscaled coefficients for a surface roughened with transverse square elements of a rib height-to-pitch ratio e/ℓ. Behavior of λ_θ with variations in e/ℓ is plotted for $\kappa = 0$ (adiabatic ribs), $\kappa \to \infty$ (isothermal ribs), and $\kappa \approx 3.66$ (wooden ribs). The typical configurations of continuous ribs described in Table 1 are indicated with dashed lines.

$$\frac{\partial \ddot{u}_i}{\partial \hat{x}_i} = 0, \tag{17}$$

$$\rho \ddot{u}_j \frac{\partial \ddot{u}_i}{\partial \hat{x}_j} = -\frac{\partial(\ddot{P} - \hat{P}_\infty)}{\partial \hat{x}_i} + \mu \frac{\partial^2 \ddot{u}_i}{\partial \hat{x}_j^2} + \rho \beta (\ddot{T} - \hat{T}_\infty) g \delta_{i1}, \tag{18}$$

$$\ddot{u}_j \frac{\partial \ddot{T}}{\partial \hat{x}_j} = \alpha \frac{\partial^2 \ddot{T}}{\partial \hat{x}_j^2}, \tag{19}$$

subject to *effective* boundary conditions of the velocity and temperature over the fictitious plane interface at $\hat{y} = 0$, which are to mimic the influence of the rough layer (located at $\hat{y} < 0$ and not resolved in the homogenized simulation) on the macroscale flow problem. These conditions are available from application of the asymptotic homogenization theory as per the detailed derivation given in Ref. [16], and they are valid provided that the microscopic and the macroscopic length scales are well-separated, that is $\epsilon = \ell/H \ll 1$. Up to first-order in terms of ϵ, the effective boundary conditions read

$$\ddot{u}_1 \Big|_{\hat{x}_2 = 0} \approx \Lambda_x \frac{\partial \ddot{u}_1}{\partial \hat{x}_2} \Big|_{\hat{x}_2 = 0} + M_{12} \frac{\rho g \beta (\hat{T}_w - \hat{T}_\infty)}{\mu}, \qquad \ddot{u}_2 \Big|_{\hat{x}_2 = 0} = 0, \tag{20}$$

$$\ddot{T} \Big|_{\hat{x}_2 = 0} \approx \hat{T}_w + \Lambda_\theta \frac{\partial \ddot{T}}{\partial \hat{x}_2} \Big|_{\hat{x}_2 = 0}, \tag{21}$$

with Λ_x, Λ_θ, and M_{12} the dimensional Navier-slip, thermal-slip, and interface permeability coefficients, respectively. These upscaled parameters can be related to their dimensionless counterparts (λ_x, λ_θ, and m_{12}) as follows:

$$\Lambda_x = \lambda_x l, \quad \Lambda_\theta = \lambda_\theta l, \quad M_{12} = m_{12} l^2. \tag{22}$$

The macroscopic coefficients λ_x and m_{12} are dependent merely on the geometric characteristics of the roughness pattern, i.e., the rib height-to-pitch ratio (e/ℓ) besides the segment length-to-pitch ratio (d/ℓ) when truncated ribs are considered, while the thermal-slip coefficient, λ_θ, also depends on the rib-to-fluid thermal conductivity ratio, κ. To evaluate these coefficients, it is sufficient to solve a Stokes-like and a Laplace-like closure problems governing the distributions of the auxiliary variables ($\ddot{u}_{i1}$, $\ddot{p}_1$) and ($\tilde{\theta}$, $\tilde{\phi}$) in an elementary cell of the microscopic domain (refer to Fig. 6(d,e)) with the dimensions/coordinates normalized by the pitch distance ($x_i = \hat{x}_i/\ell$); such *ad hoc* problems can be written, respectively, as follows:

$$\begin{cases} \partial_i \ddot{u}_{i1} = 0, \\ -\partial_i \ddot{p}_1 + \partial_j^2 \ddot{u}_{i1} = 0, \\ \ddot{u}_{i1} = 0 \quad \text{at } \mathcal{I}_{bf} \text{ and } \mathcal{I}_{rf}, \\ -\ddot{p}_1 \delta_{i2} + \partial_2 \ddot{u}_{i1} + \partial_i \ddot{u}_{21} = \delta_{i1} \quad \text{at } y = y_\infty, \end{cases} \tag{23}$$

and

$$\begin{cases} \partial_i^2 \tilde{\theta} = 0 \quad \text{in the fluid domain}, \\ \partial_i^2 \tilde{\phi} = 0 \quad \text{in the ribs}, \\ \tilde{\theta} = 0 \quad \text{at } \mathcal{I}_{bf}, \\ \tilde{\phi} = 0 \quad \text{at } \mathcal{I}_{br}, \\ \tilde{\theta} = \tilde{\phi}, \; \frac{\partial \tilde{\theta}}{\partial n} = \kappa \frac{\partial \tilde{\phi}}{\partial n} \quad \text{at } \mathcal{I}_{rf}, \\ \partial_2 \tilde{\theta} = 1 \quad \text{at } y = y_\infty, \end{cases} \tag{24}$$

plus periodicity of all the dependent variables in the x and z directions. Note that $\partial_i = \frac{\partial}{\partial x_i}$ and $\partial_i^2 = \frac{\partial^2}{\partial x_i^2}$. Once the closure variables $\ddot{u}_{11}$ and $\tilde{\theta}$ are available by conducting numerical simulations with the matching interface, at $y = y_\infty$, set sufficiently far from the wall ($y_\infty \approx 5$ is commonly accepted), the macroscopic coefficients for a matching interface of choice at $y_\infty = 0$, i.e., the plane passing through the outer edges of the ribs, can be estimated directly from the following averaging relations:

$$\lambda_x = \frac{1}{\mathcal{A}_{xz}} \int_{S_0} \ddot{u}_{11} \, dA, \quad m_{12} = \frac{1}{\mathcal{A}_{xz}} \int_{\mathcal{V}_0} \ddot{u}_{11} \, dV, \quad \lambda_\theta = \frac{1}{\mathcal{A}_{xz}} \int_{S_0} \tilde{\theta} \, dA, \tag{25}$$

with S_0 and $\mathcal{V}_0$ the virtual surface at and the fluid volume below the plane $y = 0$, respectively, and $\mathcal{A}_{xz}$ the area of an $x - z$ cross section of the elementary cell (normalized by ℓ^2); $\mathcal{A}_{xz} = 1 \times \frac{2d}{\ell}$ for the case of truncated ribs. A parametric study of the dependence of the model coefficients on the characteristics of the roughness pattern has been performed, and the results for continuous and truncated ribs are presented in Figs. 7 and 8, respectively.

The homogenization-based numerical simulations were conducted with focus on the evaluation of the surface-averaged Nusselt number, to be validated against the corresponding results of the full fine-grained simulations. Since the virtual interface chosen at $\hat{x}_2 = 0$ is smooth and impermeable, the average Nusselt number can be simply calculated from the following relation:
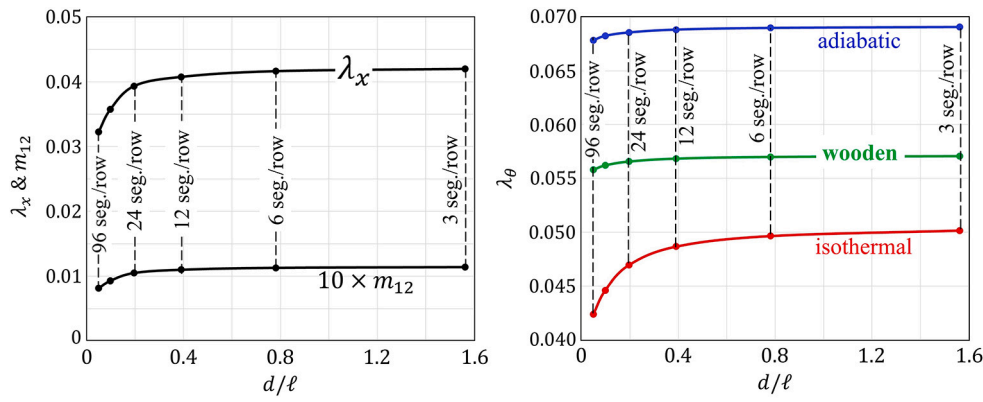
Fig. 8. Model coefficients for a surface roughened with a staggered pattern of truncated elements having a rib height-to-pitch ratio of 0.0625, and a segment length-to-pitch ratio d/ℓ. The dependence of λ_θ on d/ℓ is shown for $\kappa = 0$ (adiabatic ribs), $\kappa \to \infty$ (isothermal ribs), and $\kappa \approx 3.66$ (wooden ribs). Dashed lines indicate the typical configurations of truncated ribs described in Table 1, and additional two with larger number of seg./row.

$$\left. \overline{Nu} \right|_{homog.} = \frac{1}{H} \int_{\hat{x}_1=0}^{\hat{x}_1=H} \left. Nu \right|_{homog.} d\hat{x}_1, \tag{26}$$

with the Nusselt number $\left. Nu \right|_{homog.}$ defined locally at any point on the virtual interface as follows:

$$\left. Nu \right|_{homog.} = \frac{-H}{\hat{T}_w - \hat{T}_\infty} \times \left. \frac{\partial \ddot{T}}{\partial \hat{x}_2} \right|_{\hat{x}_2=0}. \tag{27}$$

It was explained in Ref. [16] that the predictions of the homogenized model for the Nusselt number can deviate significantly from the accurate values close to the leading edge of the vertical plate; here, we follow the same technique adopted and validated by Ahmed et al. [16] to alleviate this problem. Accordingly, the results of $\left. Nu \right|_{homog.}$ over an initial distance of the virtual interface, indicated here as the correction distance $(\hat{x}_{corr.})$, are replaced by the corresponding values of Nu over an isothermal flat surface when calculating $\left. \overline{Nu} \right|_{homog.}$ from Eq. (26). Such a distance was chosen in Ref. [16] as

$$\hat{x}_{corr.} = 2\ell \left(1 - \frac{3}{\ell/e + 2} \right). \tag{28}$$

4. Results and discussion

Results for the local and the average Nusselt numbers over the heated vertical surface, based on the experiments carried out with different roughness patterns (continuous/truncated ribs; cf. Table 1) and the full feature-resolving CFD simulations, are presented, discussed, and compared in this section, together with predictions of the homogenization-based numerical simulations.

4.1. Local heat transfer: experimental and numerical results

Experimental results of the local Nu over the heated surface (on which spanwise-elongated ribs are arranged) are plotted versus the normalized vertical coordinate $X = \hat{x}/H$ in Fig. 9(left), while the corresponding trends obtained from the fine-grained simulations are displayed in Fig. 9(right). To facilitate the readability of the figure, the experiments with continuous ribs are grouped into Groups A, B, and C, each of which encompasses three different ribbed configurations, for instance, A1, A2, and A3 (and likewise for B and C); configuration no. 2 (respectively 3) is obtained simply by introducing an additional rib between each two adjacent ribs in configuration no. 1 (respectively 2) of the same group (see Table 1). The measured/calculated values of Nu are related only to the inter-rib regions of the baseplate surface. While results of the CFD simulations indicate marked reductions of Nu over

the baseplate zones located immediately upstream and downstream of ribs (due to the separation eddies which cause local thickening of the thermal boundary layer; cf. the visualizations/comments in Refs. [14–16]), experiments were unable to capture such effects due to some limitations on the optical accessibility to these regions. Despite this, the agreement between measured and calculated results is satisfactory; the outcomes of both approaches show that attaching continuous ribs to the heated surface has, in general, a negative impact on the convective heat transfer from the inter-rib spaces, except for specific spots located in the central regions of the inter-rib spaces, where the heat transfer performance may improve locally provided that the rib density over the heated plate is relatively low (i.e., for values of ℓ/e larger than about 10). These findings are consistent, at least from a qualitative point of view, with the local Nusselt number behaviors observed in Ref. [8].

The experimental-numerical comparison for local Nu distributions in the presence of truncated ribs is presented in Fig. 10, where the results are provided only over the free baseplate spaces between rib rows. Spanwise-averaged values of Nu (i.e., averaged over a line extending in $\hat{z}$) are reported at each vertical position, $X = \hat{x}/H$. In previous activities carried out at relatively higher Rayleigh numbers (of order 10^8) [8,13], attaching staggered truncated ribs to a heated vertical surface was found capable of enhancing the heat transfer performance throughout the majority of the inter-row spaces; it was conjectured that this favorable effect is due to the ability of truncated ribs to induce local instabilities close to the edges of each segment (first signs of transition to turbulence) when the Rayleigh number is close to (but hasn't reached yet) the transitional one for a corresponding smooth surface. In contrast, the present experimental and numerical activity is conducted at flow conditions ($Ra \approx 2 \times 10^7$) well within the laminar regime even when the ribs are introduced, as inferred based on numerous schlieren visualizations. This may justify why the corresponding experimental and numerical results in Fig. 10 (again in substantial agreement with each other) do not reveal any advantage in terms of the values of Nu along each inter-rib region, relative to the smooth plate case.

While the fully featured distributions of the local Nusselt number over the plate surface, including variations in the spanwise direction $\hat{z}$, are not obtainable via the imaging technique employed in the experiments, they are available from the fine-grained CFD simulations; these results can provide better insight into the influence of truncated ribs on the convective heat transfer from the baseplate surface. In Fig. 11, contours of the Nusselt number are displayed in the presence of the three different configurations considered for truncated ribs (i.e., by varying the element length), and, for more elaboration, plots of Nu along vertical lines passing either through the middle of the segments or close to their side surfaces are shown. From inspection of the figure, it is evident that heat transfer from the baseplate peaks in the vicinity of flow regions where the fluid stream is redirected (significantly deflected in
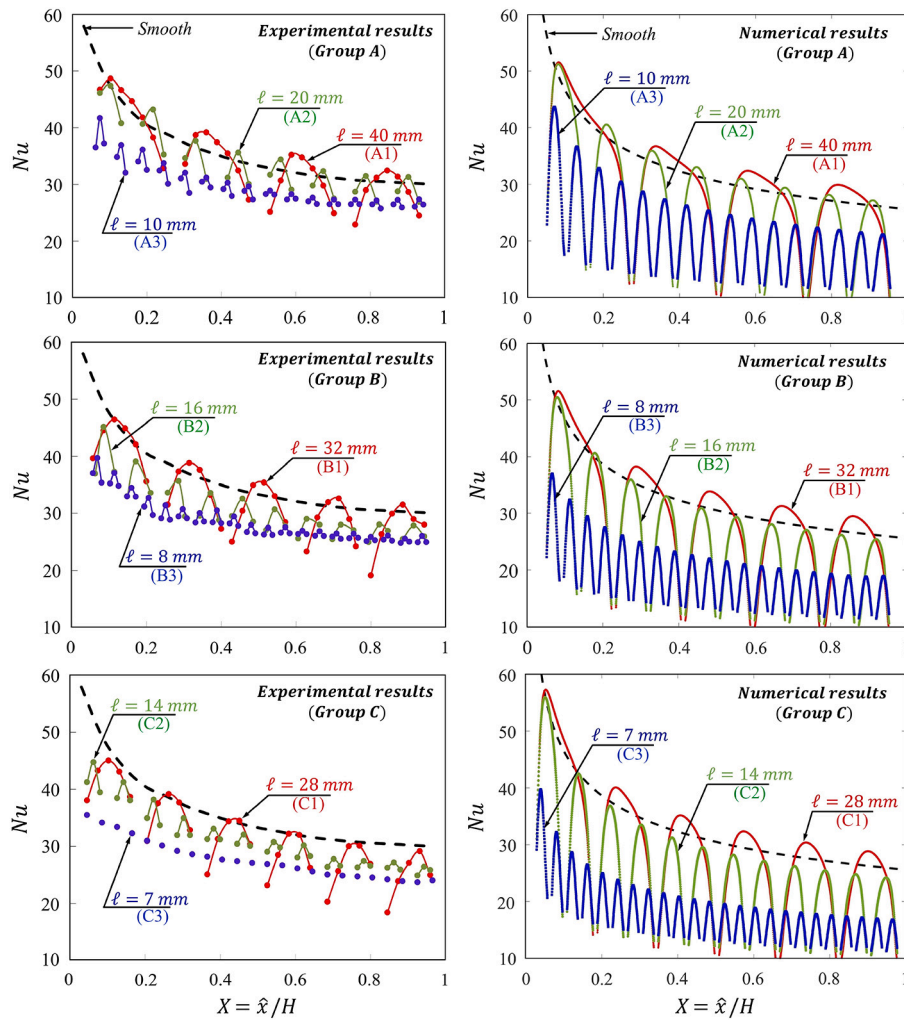
Fig. 9. Local Nusselt number distributions along the vertical heated plate when continuous (spanwise-elongated) ribs are attached to the surface; typical geometric characteristics of the different configurations considered are available in Table 1.
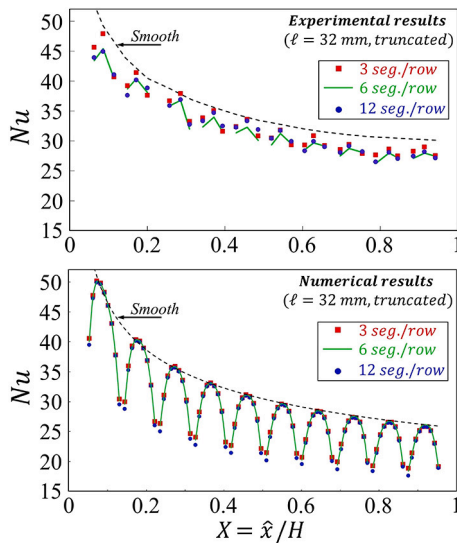

Fig. 10. Experimental results (top) and numerical predictions (bottom) for the local Nusselt number along the vertical heated plate when truncated ribs are attached to the surface.

the spanwise direction) due to the effect of rib truncation on the velocity field (cf. plots along lines II and IV); in addition, a local peak of Nu

is observed in the central spot between each two ribs belonging to successive similar rows (cf. plots along lines I and III). An in-depth look at the contours of Nu reveals that, when the segment length is larger (i.e., with smaller number of segments per row), the following effects are encountered: the regions of local heat transfer maximization associated with deflection of the fluid stream are fewer (adverse effect), yet the levels of Nu in these regions, and also in the central spots between ribs of each two successive similar rows, are higher (favorable effect) compared with the case of the shortest segments. The aforementioned opposing effects, and others that may arise from the complex dynamic and thermal interaction between the flowing fluid and the protrusions, can justify the similarity between the Nusselt number trends over the different surfaces when the analysis is conducted on a line average basis (as in Fig. 10) or when the surface-averaged values are compared (as presented next).

4.2. Overall heat transfer: experimental and numerical results

Trends of the average convective and radiant Nusselt numbers, defined respectively by Eqs. (5) and (6) with the corresponding heat transfer rates evaluated via experimental energy balance estimations and analytical analysis of radiation (refer to Section 2.2), are plotted in Fig. 12 as functions of the equivalent number of rib rows ($N_{rows,eq.}$) for the different configurations under study, that is, the typical number of rows ($= N_{rows}$, from 5 to 25) in the case of continuous ribs and
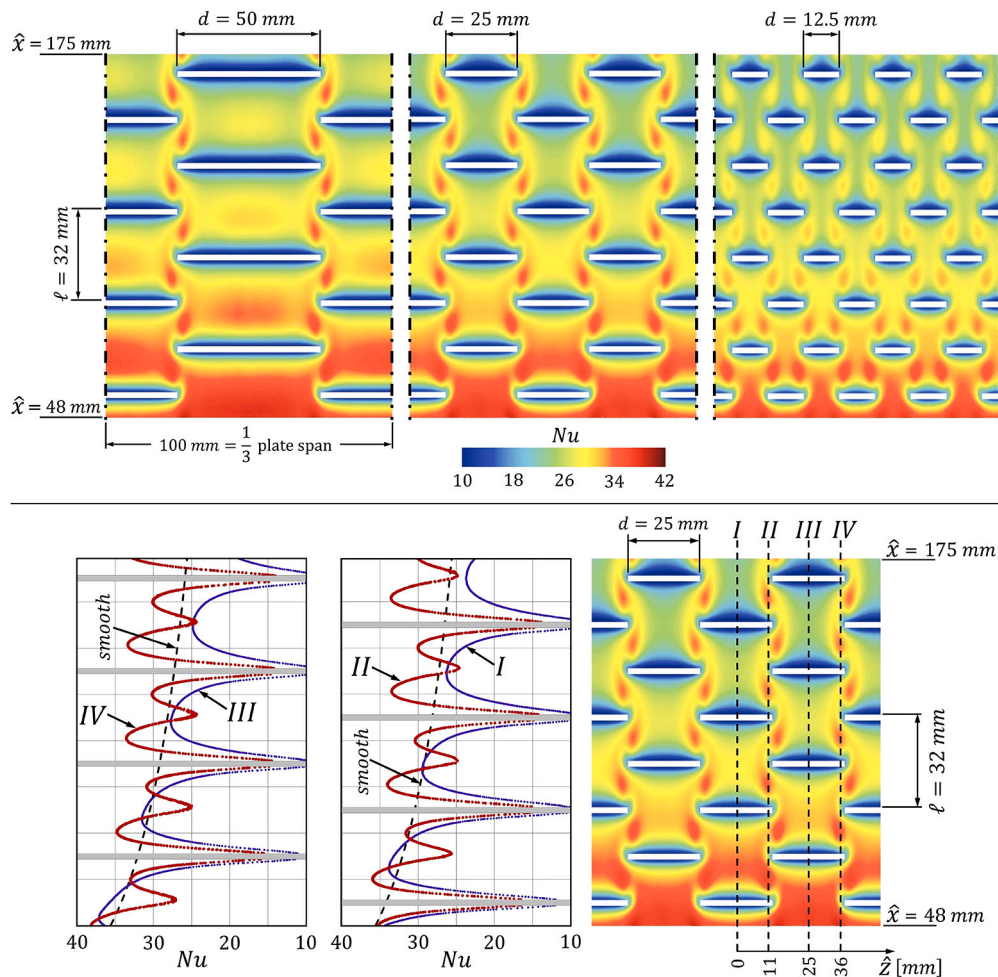
Fig. 11. Numerical predictions for the fully featured results of Nu, displayed over an upper portion of the baseplate surface when truncated ribs are attached. The regions shown have spanwise lengths equal to one-third of that of the plate; hence, overall, the roughness patterns consist of (from top left to top right) 3, 6, and 12 segments/row, as presented in Table 1.
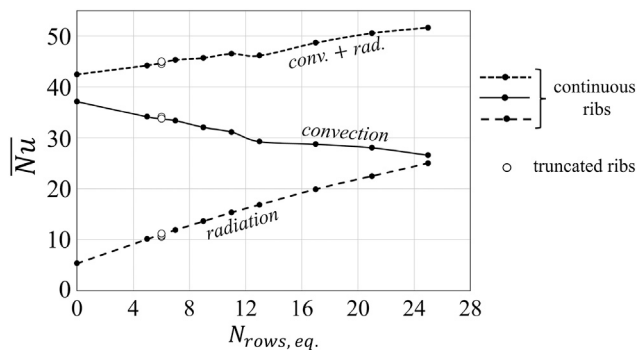

Fig. 12. Experimental results for the convective and the radiant average Nusselt numbers (and their summation) over the vertical surface, plotted against the equivalent number of rib rows ($N_{rows,\,eq.}$) for the different configurations under study.

approximately half the number of rows in the case of truncated ones ($\approx N_{rows}/2$). The following behaviors can be observed from the figure:

(i) The convective heat transfer rate decreases monotonically with the increase of the number of continuous ribs attached to the heated plate. In particular, the average convective Nusselt number drops from about 37.1 (in the absence of ribs) to almost 26.6 (when 25 ribs are present), thus deteriorating by more than 28%.

This result is in line not only with the local heat transfer measurements in Fig. 9 but also with previous literature works reporting a general convective heat transfer degradation by adding the continuous ribs notwithstanding the associated increase in the heat transfer area [7–9].

(ii) The estimated radiant component dramatically increases (up to more than 400%) with the ribs becoming densely packed on the heated vertical plate due to increased surface area at relatively large thermal emittance (0.9 for wooden ribs' surfaces against 0.12 for aluminum baseplate surface).

(iii) The overall heat transfer rate (convection plus radiation) increases by up to 22% as the number of rib rows increases, thanks to the significant enhancement in the radiant component which outweighs the decline in the convective one.

(iv) The convective, the radiant, and thus the overall heat transfer rates in the presence of truncated ribs are the same as in the case of continuous ribs having the same number of equivalent rows ($N_{rows,eq.}$), and thus almost half the typical number of rows (N_{rows}). For more clarity, the heat transfer performance with 11 rows of truncated ribs (regardless of the number of segments per row) was found comparable to that with 6 continuous ribs, taking into account that the extra surface area introduced by ribs is almost the same in both cases.

The present findings draw attention to applications in which rib-like components are fixed on a heated surface to perform specific functions
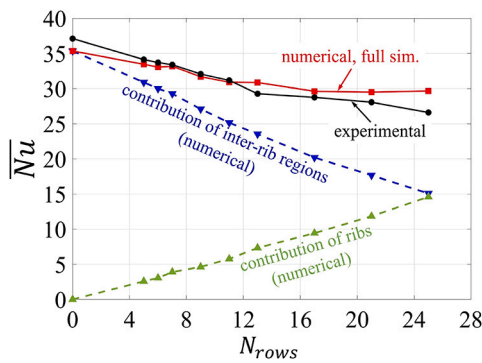
Fig. 13. Comparison between experimental and numerical results for the average convective Nusselt number with changes in the number of continuous ribs attached to the vertical surface.

Fig. 14. Comparison between predictions of the homogenized simulations (dashed lines) and of the reference fine-grained ones (thin solid lines with symbols) for $\overline{Nu}$ over the vertical heated surface in the presence of continuous ribs.

related to the operation of interest (for instance, electronic devices on a chip). In such situations, if the attached components are, for instance, of low emittance, and thus natural convection remains the only heat transfer regime of significance, the heat dissipation from the system is expected to degrade; therefore, the maximum allowable power supply is to be reduced, otherwise the operating temperature can exceed its permissible limit.

Now, the focus shifts to the comparison between the experimentally obtained values of the average convective Nusselt number (see Eq. (5)) and the predictions of the feature-resolving CFD simulations (see Eqs. (13) to (15)) to validate the latter. Fig. 13 shows that, for the different configurations of continuous ribs, experimental and numerical results of $\overline{Nu}$ are in reasonable agreement, where deviations between the corresponding values are in general within $\pm 5\%$, with a maximum of about 12% observed for the densest roughness pattern (i.e., $N_{rows} = 25$), possibly due to experimental uncertainty in estimation of $\overline{Nu}$ which is more significant ($\pm 14\%$) for such a large number of ribs, as elaborated earlier in Section 2.3. The separate roles (numerically calculated) played by convection from the inter-rib portions of the baseplate and from the ribs' surfaces (by using either of the two heat transfer rates to define a corresponding Nusselt number as per Eq. (5)) are shown in the figure, with the latter equalizing the former when the largest number of ribs, here explored, is approached. Furthermore, the numerical results for truncated ribs were evaluated (not plotted in the figure) and were validated against the experimental ones. Both approaches indicate minor variations in $\overline{Nu}$ among the three patterns considered (as the number of segments/row changes): the average convective Nusselt number ranges from 33.30 to 33.42, according to the simulations, and from 33.76 to 34.13, based on the experiments.

4.3. Homogenization-based calculated results

The homogenization-based approach that aims to macroscopically mimic the effect of ribs on the buoyant flow and on the overall convective heat transfer from the heated surface, employing the effective boundary conditions elaborated in Section 3.2, is validated here against the fine-grained simulations.

Spanwise-elongated ribs are considered in Fig. 14, where the model predictions for the average convective Nusselt number, $\overline{Nu}$, and the consequent percentage change in the convective heat transfer rate (relative to the smooth surface case), $\mathcal{D}\%$, are validated against results of the reference feature-resolving simulations of the nine continuous-rib patterns described in Table 1. Since the plate height ($H = 175$ mm) and the rib height ($e = 2$ mm) are fixed, the rib pitch (ℓ) and the rib height-to-pitch ratio (e/ℓ) corresponding to each value of H/ℓ (the horizontal axis of Fig. 14) can be easily calculated. In addition, while all the laboratory experiments on the roughened surface were performed with wooden ribs ($\kappa = \dfrac{k_{rib}}{k_{air}} \approx 3.66$) on account of their low cost, ease
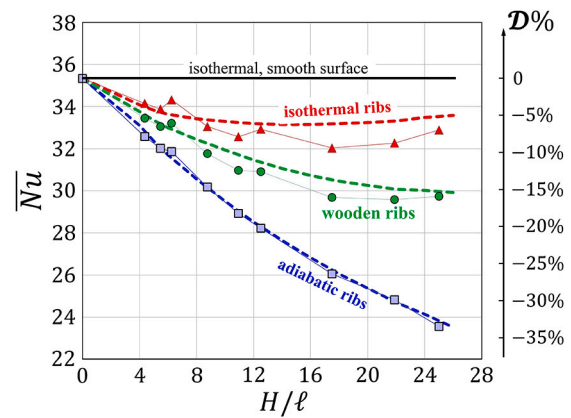
of cutting and application, and thus suitability for systematic studies on the effects of varying the geometric parameters, the homogenized and the full simulations were run also for perfectly adiabatic/conducting ribs ($\kappa = 0$ and $\kappa \to \infty$, respectively) as the two limiting situations of the rib-to-fluid thermal conductivity ratio. The model coefficients ($\lambda_x, \lambda_\theta, m_{12}$) contributing to the effective boundary conditions (20) and (21), and thus necessary for the homogenized simulations, were evaluated for the different values of e/ℓ and κ according to the trends plotted in Fig. 7. From inspection of Fig. 14, the following observations are drawn:

(i) Model predictions for $\overline{Nu}$ agree well with results of the full numerical simulations for adiabatic, wooden, and perfectly conducting ribs, and over the whole range of H/ℓ here explored.

(ii) Under the geometric and flow conditions considered, surfaces roughened with highly conducting ribs outperform (in terms of overall convective heat transfer) those having the same height and ribbed with wooden or adiabatic elements of the same size and pitch. Nevertheless, even when perfectly conducting ribs are used, the total heat transfer rate by convection (from the baseplate and ribs' surfaces) is less than that in the case of a corresponding smooth surface (i.e., in the absence of ribs), which agrees with the findings in Refs. [7,9], and can be attributed to the fact that even though conducting ribs are able to provide an extra heat transfer area, the presence of thermally inactive regions directly upstream and downstream of each protrusion, where the flow is obstructed/separated, leads to a sharp drop in the Nusselt number at these spots (associated with local thickening of the thermal boundary layer) to the extent that the overall convective heat transfer from the heated vertical surface degrades [7,9,14–16].

(iii) Although the thermal conductivity of wood ($k_{rib} \approx 0.1\,\mathrm{Wm^{-1}K^{-1}}$) is relatively low, the convective heat transfer rate with wooden ribs (of small size by definition) is intermediate between the cases of adiabatic and perfectly conducting elements having the same geometry and pitch; this is consistent with the findings in Ref. [16].

(iv) Simplifying the fine-grained simulations by assuming that low-thermal-conductivity ribs behave like adiabatic (or isothermal) ones, in order to avoid solving the conduction problem within the ribs and thus to reduce the mesh requirements, may lead to questionable results.

Predictions of the homogenized model for $\overline{Nu}$ in the case of truncated ribs (adiabatic, wooden, or isothermal) are presented in Fig. 15, with the role of the segment length-to-pitch ratio (d/ℓ) examined. The model coefficients ($\lambda_x, \lambda_\theta, m_{12}$) were estimated for the different values of d/ℓ and κ based on the behaviors shown in Fig. 8; note that the
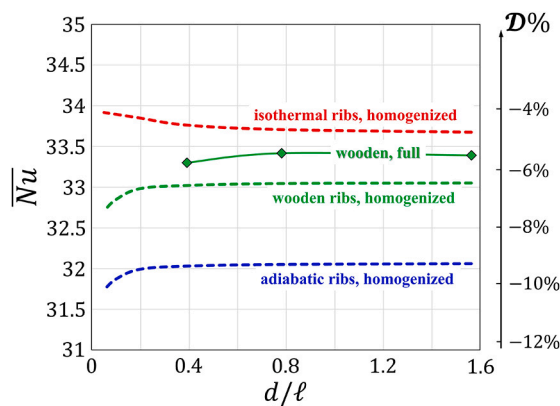
Fig. 15. Homogenization-based predictions (dashed lines) for $\overline{Nu}$ in the presence of truncated ribs, plotted against the rib length-to-pitch ratio. Results of the full fine-grained simulations for the three patterns of truncated wooden ribs described in Table 1 are also presented.

pitch distance ℓ is equal to 32 mm for all the truncated-rib patterns. When truncated wooden ribs are present, values of the average convective Nusselt number based on the model are found to be close to those obtained through the full simulations, with absolute deviations of less than 2%.

5. Conclusions

An experimental and numerical investigation of natural convection heat transfer from vertical rib-roughened surfaces under laminar regime is reported. The aim of the study was to determine whether transverse roughness elements can result in a heat transfer enhancement (relative to the smooth plate) in the laminar buoyant-flow regime. The major findings of the study are as follows:

(i) The presence of transverse continuous ribs, regularly spaced on the heated plate at a rib pitch-to-height ratio ranging from 3.5 to 20, resulted in a convective heat transfer degradation, from both local (for the plate regions not occupied by ribs) and overall (baseplate and ribs) perspectives; local heat transfer was found to be higher than the corresponding one for the smooth plate only for some spots located in the central region of the inter-rib space, exclusively when the rib pitch-to-height ratio is larger than about 10.

(ii) Truncating the ribs into segments arranged in a staggered pattern on the vertical surface, a practice found beneficial to heat transfer enhancement, relative to the smooth plate, in previous investigations [8,13] conducted at a relatively high Rayleigh number (of order 10^8), did not provide any advantage in the present study where the Rayleigh number is relatively low (of order 10^7, ensuring stable flow). From an average point of view, they performed as a continuous rib configuration having a pitch double that of the truncated one.

(iii) All the circumstances above were confirmed via both conventional fine-grained CFD simulations of the conjugate heat transfer problem (conduction through ribs and convection from ribs' surfaces and inter-rib baseplate portions to air) and homogenization-based ones which exploit effective boundary conditions to macroscopically mimic the phenomena, thus simplifying the numerical work by bypassing resolution of the fields through/between/in close vicinity of the ribs.

(iv) Results of the numerical simulations showed that the heat transfer rate from surfaces roughened with wooden ribs ($k_{rib} \approx 0.1$ $Wm^{-1}K^{-1}$) may differ significantly from those roughened with perfectly adiabatic ones, especially when the ribs are densely packed on the wall. In particular, their performance was found

intermediate between the cases of adiabatic and perfectly conducting elements, which implies that adopting the latter simplifications may lead to questionable results.

CRediT authorship contribution statement

Essam Nabil Ahmed: Writing – review & editing, Writing – original draft, Visualization, Validation, Software, Methodology, Investigation, Formal analysis, Data curation, Conceptualization. **Giovanni Tanda:** Writing – review & editing, Writing – original draft, Visualization, Validation, Supervision, Project administration, Methodology, Investigation, Formal analysis, Data curation, Conceptualization.

Declaration of competing interest

The authors declare that they have no known competing financial interests or personal relationships that could have appeared to influence the work reported in this paper.

Data availability

Data will be made available on request.

References

[1] F.P. Incropera, Convection heat transfer in electronic equipment cooling, ASME J. Heat Transf. 110 (4b) (1988) 1097–1111, https://doi.org/10.1115/1.3250613.

[2] B. Nghana, F. Tariku, G. Bitsuamlak, Numerical assessment of the impact of transverse roughness ribs on the turbulent natural convection in a BIPV air channel, Build. Environ. 217 (2022) 109093, https://doi.org/10.1016/j.buildenv.2022.109093.

[3] M. Bohn, R. Anderson, Heat-transfer enhancement in natural convection enclosure flow, Report No. SERI/TR–252-2103, Solar Energy Research Institute, Golden, CO, USA, 1984, https://doi.org/10.2172/6480292.

[4] S.E. Gilani, H.H. Al-Kayiem, D.E. Woldemicheal, S.I. Gilani, Performance enhancement of free convective solar air heater by pin protrusions on the absorber, Sol. Energy 151 (2017) 173–185, https://doi.org/10.1016/j.solener.2017.05.038.

[5] C.P. Tzanos, J.H. Tessier, D.R. Pedersen, An optimization study for the reactor vessel auxiliary cooling system of a pool liquid-metal reactor, Nucl. Technol. 94 (1) (1991) 68–79, https://doi.org/10.13182/NT91-A16222.

[6] J. Hærvig, H. Sørensen, Natural convective flow and heat transfer on unconfined isothermal zigzag-shaped ribbed vertical surfaces, Int. Commun. Heat Mass Transf. 119 (2020) 104982, https://doi.org/10.1016/j.icheatmasstransfer.2020.104982.

[7] S.H. Bhavnani, A.E. Bergles, Effect of surface geometry and orientation on laminar natural convection heat transfer from a vertical flat plate with transverse roughness elements, Int. J. Heat Mass Transf. 33 (5) (1990) 965–981, https://doi.org/10.1016/0017-9310(90)90078-9.

[8] G. Tanda, E.N. Ahmed, A. Bottaro, Natural convection heat transfer from a ribbed vertical plate: effect of rib size, pitch, and truncation, Exp. Therm. Fluid Sci. 145 (2023) 110898, https://doi.org/10.1016/j.expthermflusci.2023.110898.

[9] G. Tanda, Natural convection heat transfer in vertical channels with and without transverse square ribs, Int. J. Heat Mass Transf. 40 (9) (1997) 2173–2185, https://doi.org/10.1016/S0017-9310(96)00246-3.

[10] L.-S. Yao, Natural convection along a vertical complex wavy surface, Int. J. Heat Mass Transf. 49 (1–2) (2006) 281–286, https://doi.org/10.1016/j.ijheatmasstransfer.2005.06.026.

[11] T. Fujii, M. Fujii, M. Takeuchi, Influence of various surface roughness on the natural convection, Int. J. Heat Mass Transf. 16 (3) (1973) 629–636, https://doi.org/10.1016/0017-9310(73)90228-7.

[12] S.H. Bhavnani, A.E. Bergles, Natural convection heat transfer from sinusoidal wavy surfaces, Wärme- Stoffübertrag. 26 (6) (1991) 341–349, https://doi.org/10.1007/BF01591667.

[13] G. Tanda, E.N. Ahmed, A. Bottaro, Experimental observations of the onset of unsteadiness for buoyant airflow along smooth and rough vertical isothermal walls, presented at the 40th U.I.T. International Heat Transfer Conference, Assisi, Italy, 26–28 June 2023, and submitted to Experimental Heat Transfer.

[14] E.N. Ahmed, A. Bottaro, G. Tanda, A homogenization approach for buoyancy-induced flows over micro-textured vertical surfaces, J. Fluid Mech. 941 (2022) A53, https://doi.org/10.1017/jfm.2022.320.

[15] E.N. Ahmed, Natural-convection heat transfer from regularly ribbed vertical surfaces: homogenization-based simulations towards a correlation for the Nusselt number, Numer. Heat Transf., Part A, Appl. 83 (9) (2023) 991–1013, https://doi.org/10.1080/10407782.2023.2165993.

[16] E.N. Ahmed, A. Bottaro, G. Tanda, Conjugate natural convection along regularly ribbed vertical surfaces: a homogenization-based study, Numer. Heat Transf., Part A, Appl. (in press), https://doi.org/10.1080/10407782.2023.2202347.

[17] G. Tanda, Natural convection heat transfer from a staggered vertical plate array, ASME J. Heat Transf. 115 (4) (1993) 938–945, https://doi.org/10.1115/1.2911390.

[18] G. Tanda, F. Devia, Application of a schlieren technique to heat transfer measurements in free-convection, Exp. Fluids 24 (4) (1998) 285–290, https://doi.org/10.1007/s003480050175.

[19] G. Tanda, Natural convective heat transfer in vertical channels with low-thermal-conductivity ribs, Int. J. Heat Fluid Flow 29 (5) (2008) 1319–1325, https://doi.org/10.1016/j.ijheatfluidflow.2008.05.004.

[20] R.J. Goldstein, Optical techniques for temperature measurement, in: E.R.G. Eckert, R.J. Goldstein (Eds.), Measurements in Heat Transfer, second ed., Hemisphere Publishing Corporation, Washington, WA, USA, 1976 (Chapter 5).

[21] R. Siegel, J.R. Howell, Thermal Radiation Heat Transfer, third ed., Hemisphere Publishing Corporation, New York, NY, USA, 1992.

[22] A. Bejan, Heat Transfer, Wiley, New York, NY, USA, 1993.

[23] R.J. Moffat, Describing the uncertainties in experimental results, Exp. Therm. Fluid Sci. 1 (1) (1988) 3–17, https://doi.org/10.1016/0894-1777(88)90043-X.

[24] S.W. Churchill, H.H.S. Chu, Correlating equations for laminar and turbulent free convection from a vertical plate, Int. J. Heat Mass Transf. 18 (11) (1975) 1323–1329, https://doi.org/10.1016/0017-9310(75)90243-4.